MEDICAL PHYSICS

Accurate modeling and performance evaluation of a total-body pet scanner using Monte Carlo simulations

Hadi Rezaei[1,2] | Peyman Sheikhzadeh[1,3] | Pardis Ghafarian[4,5] | Habib Zaidi[6,7,8,9] | Mohammad Reza Ay[1,2]

[1]Department of Medical Physics and Biomedical Engineering, Tehran University of Medical Science, Tehran, Iran

[2]Research Center for Molecular and Cellular Imaging (RCMCI), Advanced Medical Technologies and Equipment Institute (AMTEI), Tehran University of Medical Sciences (TUMS), Tehran, Iran

[3]Department of Nuclear Medicine, Imam Khomeini Hospital Complex, Tehran University of Medical Sciences, Tehran, Iran

[4]Chronic Respiratory Diseases Research Center, National Research Institute of Tuberculosis and Lung Diseases (NRITLD), Shahid Beheshti University of Medical Sciences, Tehran, Iran

[5]PET/CT and Cyclotron Center, Masih Daneshvari Hospital, Shahid Beheshti University of Medical Sciences, Tehran, Iran

[6]Division of Nuclear Medicine and Molecular Imaging, Geneva University Hospital, Geneva, Switzerland

[7]Geneva University Neurocenter, Geneva University, Geneva, Switzerland

[8]Department of Nuclear Medicine and Molecular Imaging, University of Groningen, University, Medical Center Groningen, Groningen, Netherlands

[9]Department of Nuclear Medicine, University of Southern Denmark, Odense, Denmark

Correspondence
Habib Zaidi, Geneva University Hospital, Division of Nuclear Medicine and Molecular Imaging, CH-1211 Geneva, Switzerland.
Email: habib.zaidi@hcuge.ch

Mohammad Reza Ay, Department of Medical Physics and Biomedical Engineering, Tehran University of Medical Science, Tehran, Iran.
Email: mohammadreza_ay@tums.ac.ir

Abstract
Background: The limited axial field-of-view (FOV) of conventional clinical positron emission tomography (PET) scanners (~15 to 26 cm) allows detecting only 1% of all coincidence photons, hence limiting significantly their sensitivity. To overcome this limitation, the EXPLORER consortium developed the world's first total-body PET/CT scanner that significantly increased the sensitivity, thus enabling to decrease the scan duration or injected dose.

Purpose: The purpose of this study is to perform and validate Monte Carlo simulations of the uEXPLORER PET scanner, which can be used to devise novel conceptual designs and geometrical configurations through obtaining features that are difficult to obtain experimentally.

Methods: The total-body uEXPLORER PET scanner was modeled using GATE Monte Carlo (MC) platform. The model was validated through comparison with experimental measurements of various performance parameters, including spatial resolution, sensitivity, count rate performance, and image quality, according to NEMA-NU2 2018 standards. Furthermore, the effects of the time coincidence window and maximum ring difference on the count rate and noise equivalent count rate (NECR) were evaluated.

Results: Overall, the validation study showed that there was a good agreement between the simulation and experimental results. The differences between the simulated and experimental total sensitivity for the NEMA and extended phantoms at the center of the FOV were 2.3% and 0.0%, respectively. The difference in peak NECR was 9.9% for the NEMA phantom and 1.0% for the extended phantom. The average bias between the simulated and experimental results of the full-width-at-half maximum (FWHM) for six different positions and three directions was 0.12 mm. The simulations showed that using a variable coincidence time window based on the maximum ring difference can reduce the effect of random coincidences and improve the NECR compared to a constant time coincidence window. The NECR corresponding to 252-ring difference was 2.11 Mcps, which is larger than the NECR corresponding to 336-ring difference (2.04 Mcps).

Conclusion: The developed MC model of the uEXPLORER PET scanner was validated against experimental measurements and can be used for further assessment and design optimization of the scanner.

1 | INTRODUCTION

The axial field-of-view (AFOV) of conventional clinical whole-body PET scanners varies from 15 to 26 cm.[1,2] To obtain an acceptable signal-to-noise ratio (SNR) and image quality, each bed-position should be scanned for 2–3 min, thus enabling whole-body scanning to be performed within 10−20 min depending on patients' length.[3] In addition, PET imaging is intrinsically count-limited due to the restricted amount of injected radioactivity and the attenuation of 511 keV photons in the body before reaching the detectors of the PET scanner. Furthermore, since the major parts of the body are placed out of the AFOV, only ∼1% of the annihilation photons emitted from a human injected with a radiotracer are detected.[3] The low sensitivity causes low signal-to-noise ratio (SNR), might require higher injected activities or increased acquisition time, controversies in scanning children and pregnant women, limited advantages of dynamic imaging, and as a consequence, low patient throughput.[3,4] In conventional generation PET scanners, dynamic imaging is carried out using a sequential multi-pass protocol consisting of multi-bed acquisitions.[5] Among the limitations of this approach is that multi-bed acquisitions compromise temporal sampling resolution, and as such, capturing tracers with fast kinetics is restricted to a single-body region. Furthermore, the scanning time is divided among the multi-bed positions, and therefore the sensitivity and SNR are reduced for parametric imaging.[6] Hence, it is necessary to increase the scanner's sensitivity to some extent to address these issues. The best strategy to increase the sensitivity is to enlarge the azimuthal angle through extending the AFOV.[7]

A long axial field-of-view (LAFOV) in PET allows collecting whole-body imaging data in a single shot, which decreases dramatically the acquisition time compared to current PET scanners. A high sensitivity allows acquiring dynamic and low-dose scans suitable for PET imaging in children and pregnant women.[8] In addition, it enables dynamic total-body imaging covering all organs simultaneously in a single acquisition.[3,9] Despite the advantages of total-body PET, their conceptual design and clinical implementation faces a number of challenges. These challenges include high random coincidence rate, parallax errors, and high cost.[10,11]

Monte Carlo simulations are widely used for modeling medical imaging devices, and can be employed to investigate the effects of different scanning parameters on the performance of different PET instrumentation designs and resulting image quality.[12–17] A number of simulation studies focused on total-body PET scanners.

Poon et al. simulated a total-body PET scanner with an AFOV of 200 cm using SimSET and reported that the Noise Equivalent Count Rate (NECR) was 25−50 times greater than that of conventional PET scanners.[18] Crespo et al. simulated a 2.4 m AFOV PET scanner using Geant4 and showed that the sensitivity of total-body PET was 4.5 times greater than that of conventional PET scanners with or without time-of-flight (TOF).[19] Isnaini et al. used the GATE Monte Carlo package to compare the sensitivity and count rate performance of various PET scanners with various AFOVs. Their results showed that the NECR of a PET scanner with 2 m AFOV was 17.95 times larger than that of conventional PET systems.[20] Moreover, various publications reported using Monte Carlo simulations that using a LAFOV PET would boost the sensitivity.[21–26]

Furthermore, some studies evaluated the spatial resolution and lesion detectability using Monte Carlo simulations. Schmall et al. used the EGS4 Monte Carlo code to investigate the depth of interaction (DOI) of 2 m AFOV PET using two and three layers of crystals and reported that the DOI information could enhance the spatial resolution from 5.7 to 5 mm.[27] Zhang et al.[1] used the SimSET Monte Carlo code to simulate a total-body PET with 36 detector rings (AFOV of 196.6 cm) and compared its performance with a state-of-the-art PET with four detector rings (AFOV of 21 cm). Their results showed that the SNR of the total-body PET increased by 6.9-fold compared to the actual PET scanner, indicating significant improvement in image quality in the PET scanner with 36 rings compared to the one with four rings.[1] Ghabrial et al. evaluated the relevance of the NEMA NU-2 standards in a total-body PET scanner to determine whether modifications to the above referenced protocol are required for the characterization of Compton scattering in LAFOV scanners.[28] Moreover, the impact of patient body mass index on the scatter fraction estimated in the total-body scanner was investigated using series of voxel-based anthropomorphic phantoms.

In recent years, LAFOV PET scanners were developed for human imaging. This includes the first total-body PET developed by the EXPLORER consortium in collaboration with United Imaging Healthcare (UIH) in 2018 (named uEXPLORER PET) with 194 cm AFOV,[29] the PennPET Explorer with a 64 cm long AFOV developed at the University of Pennsylvania,[30] and more recently Siemens Healthineers introduced a commercial system, referred to as the Biograph Vision Quadra, with an AFOV of 106 cm.[31] In this work, we present an accurate Monte Carlo model of the uEXPLORER total-body PET scanner and its validation through comparison of simulated and experimentally measured performance

TABLE 1   Total-body uEXPLORER PET design parameters.

Ring diameter	78.6 cm
Axial FOV	194 cm
Crystal material	LYSO
Crystal element size	2.76×2.76×18.1 mm^3
Crystal pitch	2.85 mm×2.85 mm (axial×transaxial)
Crystals per block	6×7 (axial×transaxial)
Blocks per module	14×5 (axial×transaxial)
Number of units	8 (axial direction)
Number of modules per unit	24
Energy resolution @ 511 keV	11.7 %
Energy window	430 − 645 keV
Coincidence time resolution	500 ps

parameters according to NEMA-NU2 2018 standards. This study reports on the first of accurate Monte Carlo model of the uEXPLORER PET scanner and its validation using NEMA-NU2 2018 standards performance parameters. In a LAFOV PET, there is a large number of prompts where random events contribute the major portion. To improve NECR, it is necessary to reduce the random events, which can be achieved using an optimal coincidence time window and applying a defined maximum ring difference (MRD).[8,32] Hence, we evaluated the effects of the coincidence time window and MRD on the count rate performance using the developed model.

2 | MATERIALS AND METHODS

2.1 | Monte Carlo modeling of the uEXPLORER

The uEXPLORER PET scanner simulated in this work consisted of 8 units in the axial direction with a 2.5 mm gap between them.[29] Each unit contained 24 detector modules where each module consisted of 14×5 detector blocks, with each block containing 6×7 lutetium yttrium oxyorthosilicate (LYSO). The chemical formula of LYSO crystal with a density of 7.11 g/cm^3 is $Lu_{1.8}Y_{0.2}SiO_5$. The composition of LYSO includes 71.447% of Lutetium (Lu, Z = 71), 4.034% of Yttrium (Y, Z = 39), 6.371% of Silicon (Si, Z = 14), and 18.148% of Oxygen (O, Z = 8). The crystal pitch was 2.85 mm where the dimension of each crystal was 2.76×2.76×18.1 mm^3. The scanner had a detector ring diameter of 78.6 cm with an axial and transaxial FOV of 194 and 68 cm, respectively. The coincidence time window depends on the MRD and varies from 4.5 to 6.9 ns. The uEXPLORER PET scanner's parameters are listed in Table 1.[33]

In this study, we used the Geant4 application for Tomographic Emission (GATE v9.0) Monte Carlo toolkit.[34] The first and basic step in PET scanner modeling

consists in defining the geometry according to the scanner's specifications. Figure 1 shows the simulated uEXPLORER PET and the total-body extended cardiac-torso (XCAT) phantom with a length of 177.5 cm.[35]

GATE uses Geant4 to generate the particles and then transports them through different materials by mimicking physical interactions between particles and matter. The "emlivermore_polar" physics list was employed for all simulations. The physical processes include photoelectric absorption, Compton scattering, Rayleigh scattering, multiple scattering, pair production, ionization, non-colinearity, and positron range. In this process, several pieces of information, such as position and time of the step, momentum, and energy of the track, energy deposition of the step, and interaction type were generated and detector pulses (digits) were simulated. This process represents the series of signal processing steps made up by the Digitizer. Figure 2 shows the hierarchy of the digitizer corresponding to the uEXPLORER PET configuration. This process starts with "hits" that generate optical photons from particle interactions within the detectors. The "adder," which is not shown in the figure, collects and translates photons to pulses. The "readout" modules are usually supplied with a group of sensitive detectors collecting all the pulses generated by the adder in a detector block.[36] In = other modules, such as blurring, time resolution, thresholder, and coincidence window, the values were defined to be similar to those of the uEXPLORER and mini EXPLORER PET.[29,37] In the blurring module, the energy resolution was set to 11.7% at 511 keV. The coincidence time resolution in the early design specifications of the system was 430 ps,[29] however, the TOF resolution in the actual system was measured to be around 500 ps. The *"crystalblurring"* command was used to model the efficiency of the system. To achieve the best agreement between the simulations and experimental measurements, the crystal efficiency was varied between 90% and 99%. The best fit in the total sensitivity between simulations and experimental measurements was achieved using the least squares technique[38,39] for a value of 95.7%. This step was tuned before dead time modeling.[40] The second module where a range of values was tested to achieve a count rate close to measurements was dead time. The dead time parameter was varied between 250−350 ns at the block level with a step size of 10 ns. Investigation of the effect of dead time at this stage showed that for activities less than 222 MBq, an increase or decrease of 10 ns in dead time decreased or increased the count rate by 2% on average. Using again the least squares method, the optimal dead time value that was most consistent with the experimental results corresponded to a non-paralysable value of 289.5 ns. Table 2 shows the effect of various dead times on the count rate for an activity of about 4 kBq/cc for the scatter phantom with a length of 175 cm.
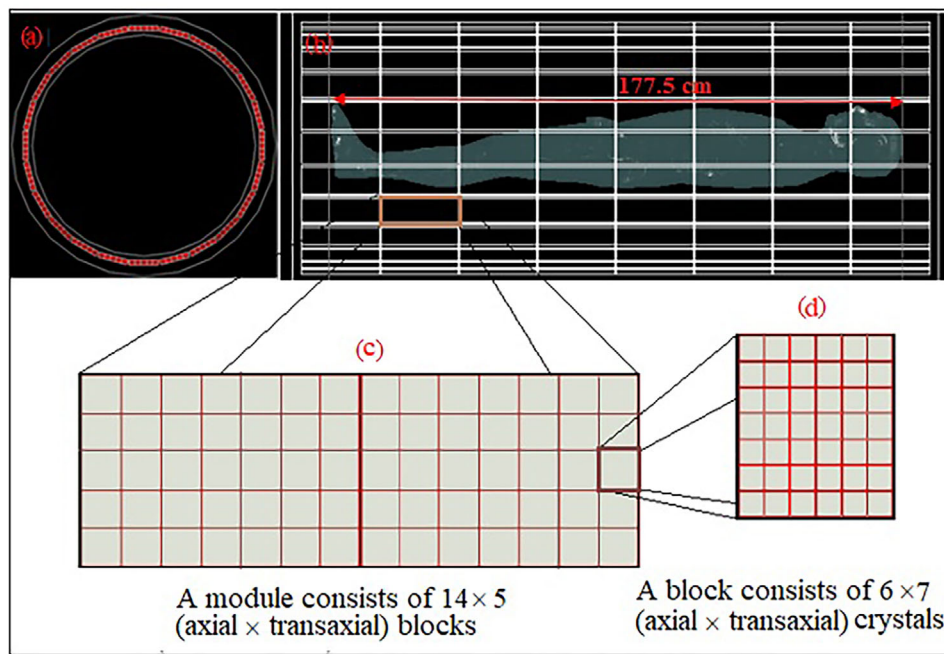
FIGURE 1 Simulated total-body PET scanner showing (a) a transaxial and (b) axial views of the uEXPLORER. (c) A module consists of 14 blocks in the axial direction and 5 blocks in the transaxial direction. (d) A block consists of six crystals in the axial direction and seven crystals in the transaxial direction.
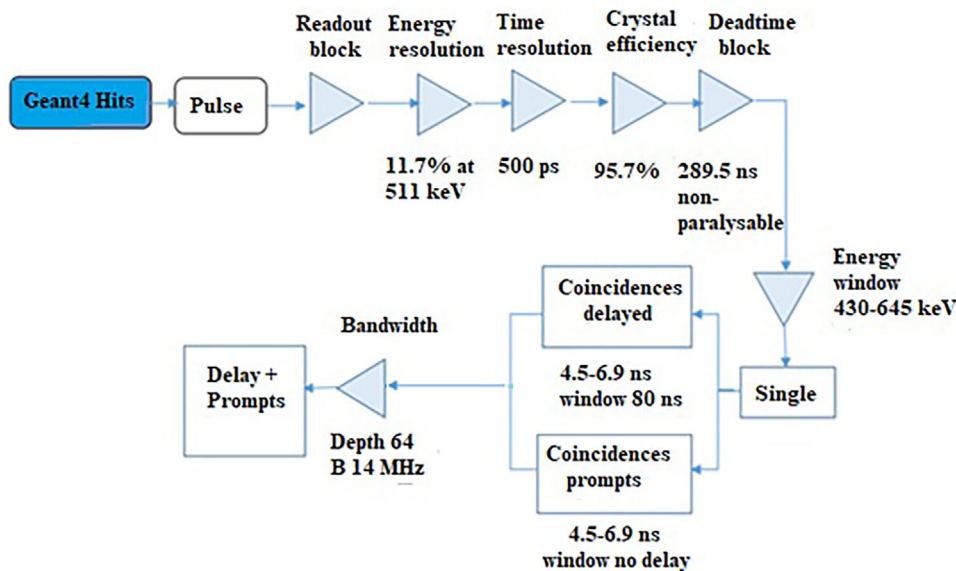

FIGURE 2 The digitizer chain of the simulated total-body PET using GATE Monte Carlo platform.

A multiple policy of *takeAllGoods* was used to imitate the behavior of coincidences. We also set the energy window from 430 to 645 keV, with the coincidence window of 4.5 ns (for 0 unit differences) and 6.9 ns (for 4 maximum unit differences). We used different coincidence windows directly in the GATE macros and employed a C++ program in post-processing to implement the unit differences.

2.2 | Validation strategy

To validate the developed model of the total-body PET scanner, a number of performance parameters were simulated and calculated based on NEMA-NU2 2018 standards and then compared with the experimental measurements reported by Spencer et al.[37]

TABLE 2 Investigation of the effect of various dead times on the count rate.

Dead time value (ns)	Trues (kcps)	Scatters (kcps)	Randoms (kcps)
250	3566	2193	2664
260	3497	2150	2612
270	3473	2108	2561
280	3438	2066	2510
290	3399	2026	2461
300	3379	1985	2412
310	3356	1945	2364
320	3226	1906	2316
330	3224	1868	2270
340	3222	1831	2225
350	3221	1794	2180

2.2.1 | Sensitivity

To calculate the sensitivity based on NEMA-NU2 2018 standards,[41] we first simulated a polyethylene phantom with 700 mm length, 2 mm inner diameter, and 3.2 mm outer diameter, filled with F-18 mixed with water. The phantom was covered by a varying number of aluminum layers. Separate simulations were carried out through adding one layer of aluminum at each step, and the sensitivity calculated accordingly. The thickness of each layer was 2.5 mm. After calculating the sensitivity of the five aluminum layers, a sensitivity curve was plotted versus the layers' thickness. Extrapolation was performed to obtain the sensitivity without attenuation. Sensitivity computations were carried out for two positions (one where the phantom was placed at the center of the FOV, and the second where the phantom was placed at 10 cm radial off-center of the FOV). A source activity of 3 MBq of F-18 was used to reduce the effects of dead-time and random coincidences. Furthermore, a polyethylene phantom (length of 1700 mm and thickness of 2 mm) without an aluminum layer filled with 3 MBq of F-18 with water was used to calculate the scanner's sensitivity.

2.2.2 | Count rate performance

To evaluate the count-rate performance, we simulated two scatter phantoms with diameter and source position similar to the phantom recommended by NEMA-NU2 2018. A 700 mm long and 6.4 mm diameter fillable line source of F-18 with water was placed at a radial distance of 4.5 mm inside a polyethylene scatter cylindrical phantom with 700 mm length and 200 mm diameter. The second was an extended scatter phantom with a length of 1750 mm in which a fillable line source similar to the first one was embedded through the length of the

phantom. Due to the large number of activity concentrations and high activity, we considered a time of 1 s for each simulation. For the 70 cm phantom, activity concentrations of 2, 4, 5, 7, 9, 10, 12, 14, 15, 16, 17, 18, and 20 kBq/cc were used, whereas for the 170 cm phantom, activity concentrations of 2, 4, 6, 8, 10, and 12 kBq/cc were used.

Furthermore, the NECR and scatter fraction (SF) were computed based on the following equations:

$$NECR = \frac{T^2}{T + S + kR} \qquad (1)$$

$$Scatter\ fraction = \frac{S}{T + S} \qquad (2)$$

where T, R, and S are the true, random, and scatter coincidences, respectively. k can be either 1 if the NECR is estimated using a low variance or 2 if delayed events are used. A k value of 1 was used in this study. The true and scatter coincidence events were estimated directly from the simulations.

2.2.3 | Randoms correction

To correct the random coincidences, the single counts in each crystal were calculated and the random events (R) estimated according to the following equation:

$$R = \frac{2\tau n_1 n_2}{T} \qquad (3)$$

where n_1 and n_2 are the single events on the two crystals which generate a line of response (LOR), 2τ is the coincidence timing window, and T is the simulation time.[42]

2.3 | Spatial resolution

2.3.1 | Point sources

To calculate the spatial resolution, six spherical point sources with a diameter of 0.5 mm located at six different positions were simulated. These point sources were centered at axial positions of zero ($z = 0$) and one-eighth AFOV and radial positions of 1, 10, and 20 cm. Each point source was filled with 300 kBq of F-18 with water and an acquisition time of 60 seconds was simulated. After the collection of about 70 million events, images were reconstructed using filtered backprojection (FBP) using a pixel size of 0.6×0.6 mm^2 (the slice thickness was 0.6 mm). The unit difference for the spatial resolution was restricted to one (24 cm).

2.3.2 | Mini-derenzo phantom evaluation

A mini-Derenzo phantom based on the experimental work published by Spencer et al.[37] was simulated to access the modeled scanner's performance. The mini-Derenzo phantom contained six rod segments with diameters of 1.2, 1.6, 2.4, 3.2, 4, and 4.8 mm filled with about 20 MBq of F-18 mixed with water. The simulation time was 60 seconds. The obtained list-mode data were reconstructed using OSEM with 20 subsets and 10 iterations. The voxel size was 1.172×1.172×1.172 mm^3.

2.4 | Effect of the coincidence time window on NECR

One of the important parameters to further reduce the number of random coincidences is the coincidence time window. In this study, we attempted to evaluate the impact of variable time window on NECR. The following equation indicates that the time window varies with the ring difference between two crystals that generate a LOR:

$$\tau\,(R) = \frac{\sqrt{T^2 + (R.W)^2}}{C} + 3.P \tag{4}$$

where R is the ring difference, T the transaxial FOV (in meters), W is the axial crystal pitch (in meters); P is the coincidence time resolution (in seconds), and C is the speed of light (in m/s). A timing resolution of 500 ps and transaxial FOV of 86 cm were set for this study.

2.5 | Image quality

To evaluate image quality of the total-body PET, the NEMA IEC phantom was simulated. A body phantom with an inner length of 180 mm was modeled. Six spheres with internal diameters of 10, 13, 17, 22, 28, and 37 and 1 mm plastic thickness were simulated. A low atomic number cylinder mimicking the lung was placed at center of the phantom. The lung has a density of 0.26 g/cm^3 and is composed of 10.3% of Hydrogen, 10.5% of Carbon, 3.1% of Nitrogen, 74.9% of Oxygen, 0.2% of Sodium, 0.2% of Phosphor, 0.3% of Sulfur, 0.3% of Chlorine, and 0.2% of Potassium. The phantom was placed at the center of the axial FOV. The spheres and the background were filled with ^{18}F and water, and the simulated acquisition time set to 5 min. The background concentration was 5.1 kBq/cc, whereas the sphere-to-background concentration ratio (SBR) was 3.7:1. The listmode data were reconstructed using the OSEM algorithm with 4 iterations and 20 subsets with resolution (point spread function—PSF)

modeling with a Gaussian filter of 3 mm FWHM, and a voxel size of 2.34×2.34×2.34 mm^3. Attenuation correction was performed and only true coincidences were considered for image reconstruction (random and scatter coincidences were removed based on GATE flags). Although geometric normalization correction can remove non-uniformity artifacts, the procedure requires simulations with high statistics to reduce noise in the reconstructed images. Moreover, calculation of the sensitivity map for the uEXPLORER PET is computationally prohibitive. In this study, normalization correction was not included.

The contrast recovery (CR) and, background variability (BV) for each sphere were calculated as follows[43,44]:

$$CR_{si} = \frac{\frac{C_{si}}{meanBK_{si}} - 1}{SBR - 1} \times 100 \tag{5}$$

$$BV_{si} = \frac{\sigma_{BK_{si}}}{meanBK_{si}} \times 100 \tag{6}$$

where C_{si} is the mean number of counts within the sphere, measured inside a region of interest (ROI) defined at the center of each sphere. meanBK$_{si}$ is the average of all background counts inside ROIs whit the same diameter of sphere i. $\sigma_{BK_{si}}$ is the standard deviation for ROIs having sphere diameters of i. SBR is the sphere-to-background concentration ratio (3.7:1). Furthermore, the relative count error in the lung (ΔC) was calculated as follows[41]:

$$\Delta C = \frac{C_{Lung}}{meanBK_{s=37}} \tag{7}$$
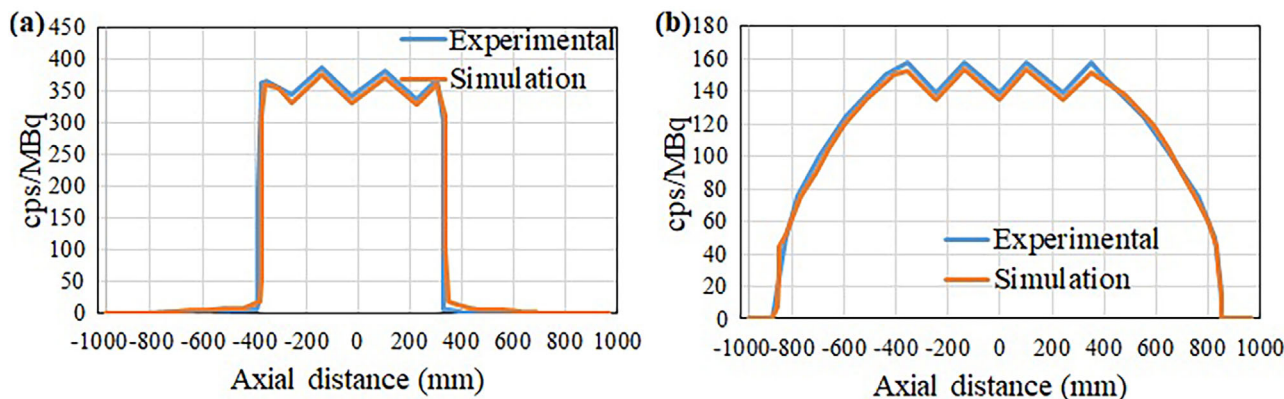
where C_{Lung} is the average counts in the ROI of 30 mm in the lung insert and, meanBK$_{s=37}$ is the average counts of the 60 ROIs of 37 mm sphere in the background.

2.6 | Computations and image reconstruction

We used GATE_v9.0 on a cluster using a high performance computing workstation with 4 CPUs (Intel Xeon CPU E7-4850v4@ 2.10 GHz), 64 cores and thus 128 threads, and 320 GB RAM DDR4. Furthermore, the ROOT output was utilized to analyze the data. For data post-processing, an in-house developed C++ code was used. Customizable and Advanced Software for Tomographic Reconstruction (CASToR) open-source software was used for OSEM image reconstruction,[45] whereas the STIR platform was used for FBP reconstruction.[46]

TABLE 3 Comparison of the total sensitivity for the 70 and 170 cm line sources at the center and at 10 cm off-center of the FOV for the simulated and experimental measurements.

Transaxial offset Position	Experimental value for 70 cm phantom (kcps/MBq)	Simulated value for 70 cm phantom (kcps/MBq)	Relative error	Experimental value for 170 cm phantom (kcps/MBq)	Simulated value for 170 cm phantom (kcps/MBq)	Relative error
0 cm	174	168	3.4%	147	144	2.0%
10 cm	177	167	5.6%	151	143	5.3%

FIGURE 3 Comparison of simulated and measured axial sensitivity profiles of the uEXPLORER PET scanner using line sources with lengths of: (a) 70 cm and (b) 170 cm.

3 | RESULTS

3.1 | Validation

3.1.1 | Sensitivity

The total sensitivity for the 70 and 170 cm phantoms was calculated and compared with the experimental values reported for the uEXPLORER PET scanner[37] at the center and at 10 cm off-center of the FOV. Table 3 summarizes the simulated total sensitivities of the 70 and 170 cm phantoms and their comparisons with the experimental results.

Figure 3 shows the sensitivity profile of the total-body PET versus the axial distance for the 70 and 170 cm phantoms for both simulations and experimental measurements. These simulated profiles are in good agreement with experimental ones. The profile indicates that the maximum sensitivity depends on the length of the line sources, where a fall-off is seen at the two ends of the line source. On the plateau of these two profiles, a number of peaks and valleys can be seen due to the selection of a $\pm$ 4 maximum unit difference. Since the total sensitivity as well as the values in the axial sensitivity profile (especially in the peak and valleys) for simulations and experimental measurements are very close to each other, the peak sensitivity for simulations is approximately equal to the experimental results. The peak

sensitivity for 170 and 70 cm line sources for simulations were 18.2% and 17.2% while they were 18.6% and 17.4%, respectively, for experimental measurements.

3.1.2 | Count rate performance

Figure 4 compares the simulated and measured true, random, and scatter coincidence count rates, as well as the NECR as a function of activity concentration in the uEXPLORER PET scanner for both 700 and 1750 mm phantoms. The simulated peak NECR for the 700 mm phantom was 1.701 Mcps at 18 kBq/cc (Figure 4b), while the experimental one was 1.524 Mcps at 17.3 kBq/cc. Furthermore, for the 1750 mm phantom the simulated peak NECR (Figure 4d) was 1.902 Mcps at 10 kBq/cc whereas the experimental value was 1.855 Mcps at 9.6 kBq/cc. Likewise; the simulated scatter fraction at the peak NECR for 700 and 1750 mm phantoms were 37% and 38.3%, respectively, while the experimentally measured values were 36.3% and 37.4%, respectively.

3.1.3 | Spatial resolution

Table 4 shows the experimental and simulated spatial resolution in the tangential, radial and axial directions
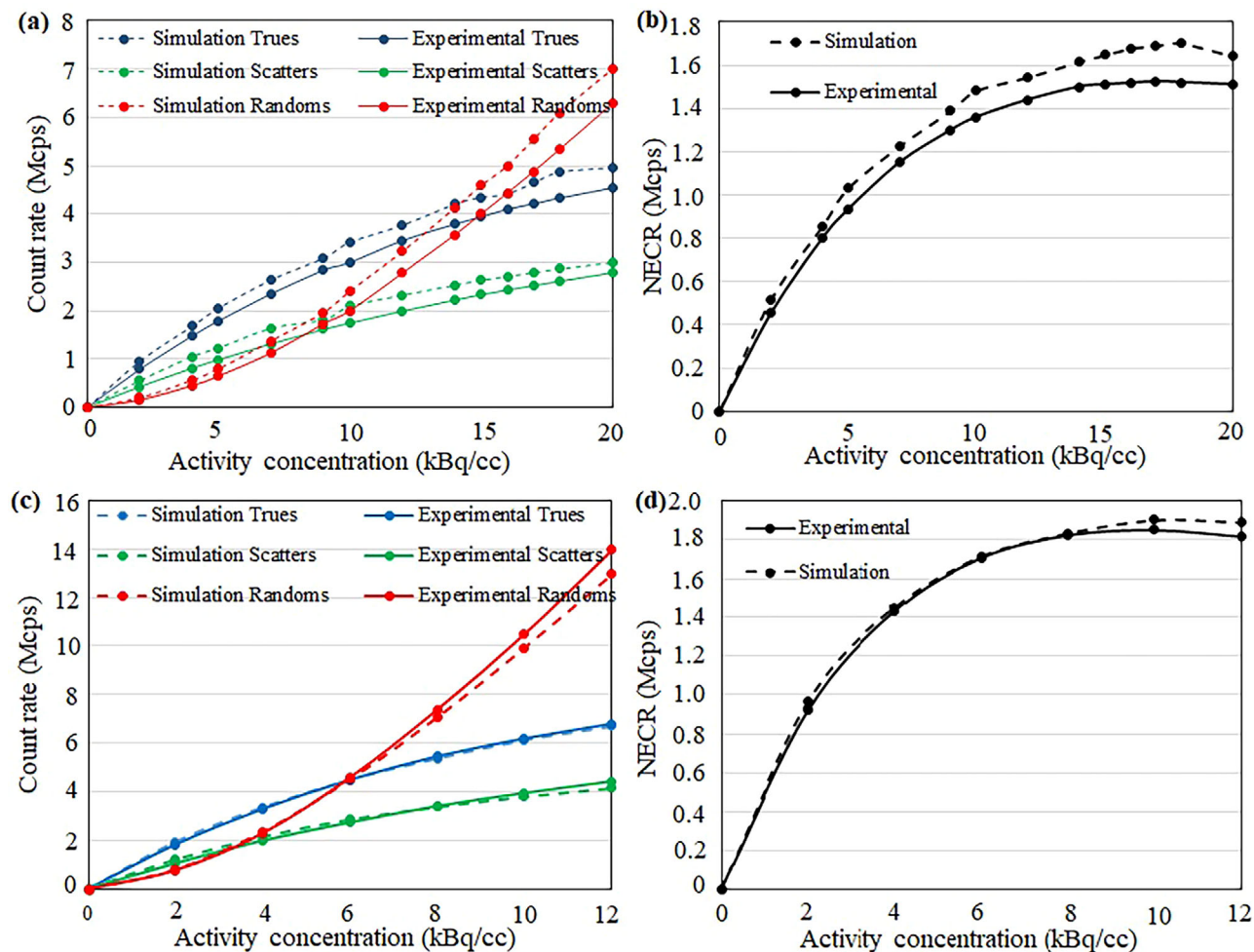
FIGURE 4 Plots comparing simulated and experimentally measured true, random, and scatter coincidence count rates for 700 mm long phantom (a) and 1750 mm long phantom (c) and NECR for 700 mm phantom (b) and 1750 mm phantom (d) for the uEXPLORER PET scanner.

TABLE 4 Comparison of experimental and simulated spatial resolution (FWHM) for point sources in the tangential, radial and axial directions at two different axial positions within the field-of-view.

| | | FWHM | | | | | | | | |
| | | Tangential | | | Radial | | | Axial | | |
Location	Position (cm)	Experimental	Simulation	Difference (mm)	Experimental	Simulation	Difference (mm)	Experimental	Simulation	Difference (mm)
Center of FOV	1	3.0	2.9	0.1	3.0	3.2	0.2	2.8	3.1	0.3
	10	3.1	3.0	0.1	3.4	3.4	0.0	3.2	3.4	0.2
	20	4.0	4.0	0.0	4.7	4.9	0.2	3.2	3.4	0.2
1/8th FOV	1	2.9	2.8	0.1	3.0	3.0	0.0	2.9	3.0	0.1
	10	3.2	3.2	0.0	3.6	3.5	0.1	3.1	2.7	0.4
	20	4.4	4.3	0.1	4.6	4.7	0.1	3.3	3.3	0.0

for six ^{18}F point sources. The average of the tangential, radial, and axial FWHM for point sources located at the center of the FOV and at radial offsets of 10, 100, and 200 mm were 3.3, 3.8, and 3.3 mm, respectively. At an axial distance of one-eighth of the FOV, the mean of the tangential, radial, and axial FWHM were 3.4, 3.8, and 3.0 mm, respectively.

Figure 5 compares the simulated and experimental reconstructed images of the mini-Derenzo phantom located at the center of the FOV.[37] The reconstruction of both images was performed using 20 subsets and 10 iterations (pixel size of 1.172×1.172 mm^2) without post-reconstruction filtering. The rods with 2.4 mm diameter were clearly visible on both images.
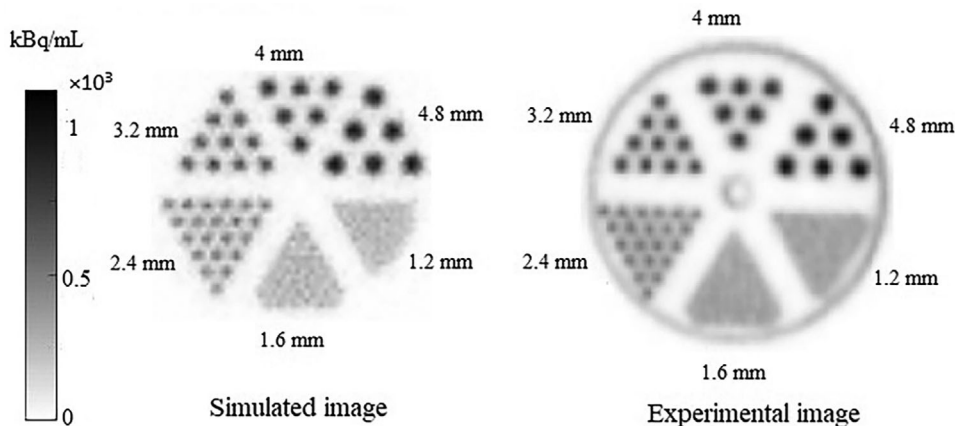
FIGURE 5 Comparison of simulated (left) and experimentally measured (right) images of the mini-Derenzo phantom on the uEXPLORER PET scanner reconstructed using OSEM algorithm with 20 subsets and 10 iterations. The experimental phantom image was reproduced with permission from Spencer et al. [37]
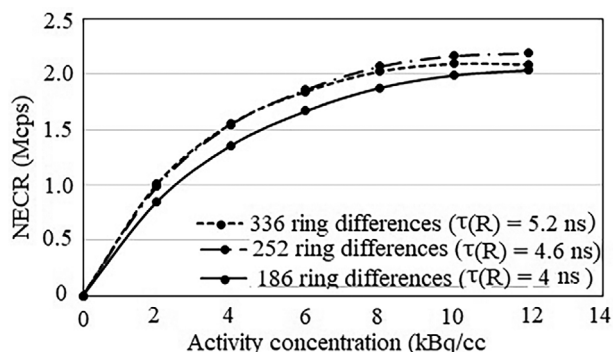

FIGURE 6 NECR as a function of activity concentration for various combinations of maximum ring difference (MRD) and coincidence time window.

3.2 | The effect of coincidence time window on the NECR

Figure 6 displays the NECR as a function of the activity concentration. For each maximum ring difference value, a time window calculated using Equation (4) is set to process all coincidence events. The results show that the NECR for a coincidence time window of 4.6 ns corresponding to 252-ring difference (three units) was 2.19 Mcps, which is larger than the NECR for 5.2 ns, which corresponds to 336-ring difference (four units) with 2.09 Mcps. This opens the option to select an optimal coincidence time window and maximum ring difference to improve the NECR.

3.3 | Image quality

Figure 7a shows a transaxial slice through the center of the six spheres of the simulated image quality phantom with resolution modeling produced by the

total-body PET scanner. Figures 7b and 7c compare the results of CR and BV, respectively, as a function of sphere size between simulations and experimental measurements for similar acquisition time (5 min). The relative count error in the lung insert amounted to 4.12% for this condition. Since we used a different image reconstruction framework, reconstructed images were evaluated at different iterations, namely, 2, 3, 4, and 5. The results achieved using four iterations were closer to the experimental report.

4 | DISCUSSION

Conventional commercial PET scanners have a maximum AFOV of 26 cm. This short AFOV relative to the length of the human body limits the sensitivity of PET scanners and increases the acquisition time. A total-body PET covers the entire body in a single shot and increases significantly the sensitivity. In addition, the injected activity and scan duration are reduced, and imaging of all organs simultaneously enabled. The uEXPLORER was the first human total-body PET scanner made commercially available.

This study aimed to develop and validate a Monte Carlo model of the uEXPLORER total-body PET scanner using the GATE simulation platform. The sensitivities defined according to the NEMA-NU2 2018 and extended phantoms were calculated at two positions. The simulated results of the 70 cm phantom were in good agreement with the experimental measurements performed on the uEXPLORER PET scanner reported by Spencer et al.[37] The relative errors between the simulated and experimental total sensitivities were 3.4% and 5.6% at the center and 10 cm off-center of the FOV, respectively. For the extended phantom with 170 cm length, the relative errors between the simulated and experimental total sensitivities were 2.0% and 5.3%
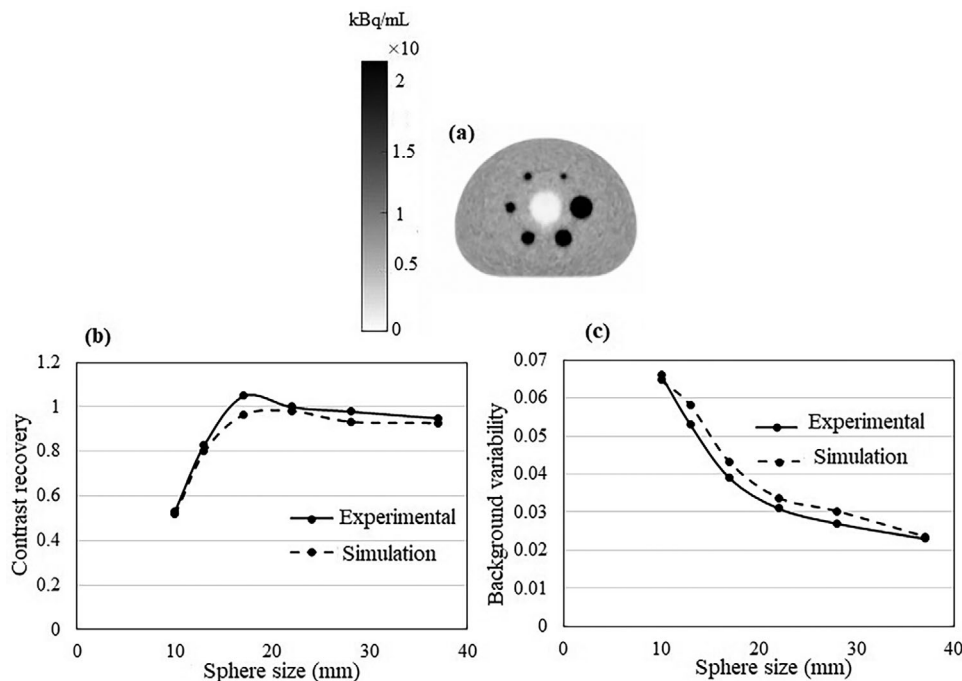
FIGURE 7 Images of the image quality phantom showing (a) a transaxial slice, (b) plots comparing the simulated and experimental CR results, and (c) plots comparing the BV results between simulations and experimental measurements. The images were reconstructed using the OSEM algorithm with 20 subsets and 4 iterations (2.34×2.34 mm^2 pixel size, with resolution modeling).

at the center and at 10 cm off-center of the FOV, respectively. These relatively small differences were expected since some electronic and digitizer parameters, such as dead-time, were not accurately modeled. In addition, pulse pile-up was not considered in this simulation. For both simulation and experimental results, the sensitivity for the 70 cm phantom is higher than the 170 cm phantom. This is due to the lower acceptance angle at the end of the scanner causing a reduced geometric efficiency at both axial edges. Hence, the rate of the true events for the 70 cm phantom is higher than the 170 cm phantom.

To evaluate the count-rate performance of the simulated total-body PET scanner, we calculated the count-rate for a phantom with a length of 700 mm based on NEMA NU-2 and an extended phantom with a length of 1750 mm. In a comparative study, Leung et al.[47] used three phantoms with lengths of 70, 175, and 210 cm and one patient. Their results indicated that the NECR of the patient was very close to that of the 175 cm phantom. Hence, an extended phantom is more suitable for the characterization of the total-body PET scanner. Figure 4 shows a good agreement between the simulated and experimentally measured plots of true, scatter, random, and NECR. The relative difference between the simulated and measured peak NECR was 11.6% and 2.5 % for the 700 and 1750 mm phantoms, respectively. The activity concentration at which the peak NECR occurred in the simulation was close to the

corresponding experimental values for both phantoms (for 700 mm phantom: 18 kBq/cc simulated versus 17.3 kBq/cc measured, for 1750 mm: 10 kBq/cc simulated versus 9.6 kBq/cc measured). Furthermore, the relative difference between the simulated and experimental results of scatter fraction was 1.9% and 2.4% for 700 and 1750 mm phantom, respectively.

A Monte Carlo study was recently carried out by Tiwari et al.[10] on an extended version of the GE Discovery MI PET scanner up to 2 m. The achieved sensitivity and peak NECR were about two times higher than those reported for the uEXPLORER. This is expected since they used thicker (25 mm) LYSO crystals compared to the uEXPLORER (18.1 mm). However, when they used 20 mm thick LYSO crystals, the sensitivity was still 1.45 times higher than the uEXPLORER. Furthermore, it should be noted that in the uEXPLORER, the maximum acceptance angle was restricted to 57°, which decreases the sensitivity, while in the extended GE study, the whole AFOV length was considered. However, since the sensitivity calculation based on NEMA is measured in attenuation-free condition, this increase in sensitivity might not reflect clinical scenario. If this calculation is performed in the presence of the patient, LORs occurring above the range of acceptance angle of 57° will be attenuated.

In terms of spatial resolution, there was a good agreement between simulated and experimental results with a difference of less than 0.4 mm, while the average bias

for all six point sources was 0.12 mm. The high sensitivity of total-body PET combined with small size crystals enables the physical realization of high spatial resolution (~3 mm) in whole-body PET imaging. The difference between simulation and experimental results can be due to differences between the experimental and simulation conditions, such as the digitizer, light transport between crystals, and the SiPMs, which were not considered in the simulation study.

Imaging of the mini-Derenzo phantom with rod diameters varying from 1.2 to 4.8 mm showed that rods with a diameter of 2.4 mm were clearly visible on both simulated and measured images. This examination also confirms the excellent agreement between the experimental and simulation results in terms of system spatial resolution.

Using variable coincidence time window as a function of maximum ring difference, according to Equation (4), could improve the count-rate performance and SNR. Minimizing the random coincidences from long LORs increases the NECR. When a large MRD is considered, it might appear that the NECR increased. While increasing the MRD increases the random and scatter coincidences. Moreover, a large MRD attenuates LORs at large acceptance angles, which reduces the true coincidence events. Therefore, choosing an optimum MRD might increase the NECR. Figure 6 showed that the NECR with a maximum ring difference of 252-rings was higher than that of the 336-rings. These results were consistent with those reported by Poon et al.[8] and Leung et al.[47]

Images of the six spheres of the image quality phantom (Figure 7a) showed that despite the short acquisition time, the contrast recovery of the spheres was high, especially for the small-size spheres (10–13 mm diameter), reflecting the high sensitivity and good spatial resolution of the uEXPLORER PET scanner. In Figure 7b, the CR of the simulated and experimental results with identical conditions (reconstruction using four iterations with PSF modeling and 5 min of time duration) are compared. For the 10 mm diameter sphere, the experimental CR is 53%, whereas it was 51.8% for the simulation study. Therefore, the relative difference between simulated and experimental results for the smallest sphere is about 2.3%. In addition, for the largest sphere, the relative difference is 2.5%. However, the average relative difference for all spheres is about 3.9%.

Figure 7c compares the BV between simulated and experimental results. The lowest and largest differences in BV were 1.8% and 11.8%, which corresponded to 10 and 28 mm spheres, respectively. The difference between simulated and experimental results can be due to differences between image reconstruction software used.

The relative count error in the lung in the simulation study was 4.12%, while it was 1.36% for experimental measurements. In addition to difference in scanning time (30 min for the real scan), this difference can be related to difference in lung material and its linear attenuation coefficient in simulated and experimental measurements.

To the best of our knowledge, this is the first study reporting on an accurate Monte Carlo model of the uEXPLORER PET scanner and its validation against experimentally measured NEMA-NU2 2018 standards performance parameters. The long AFOV of the scanner and the large number of lines of response prevented us from simulating total-body human voxel-based phantoms (e.g., XCAT).

The validated simulation model reported in this study should enable further methodological and clinical research to be performed to further optimize the conceptual design of the total-body PET scanner. Examining different TOF coincidence time resolutions and their impact on the SNR of the resulting total-body PET images is one potential avenue to explore. Likewise, evaluating different types of crystals on the performance of the total-body PET and choosing the optimal crystal in terms of efficiency and cost is also of interest. Investigating the potential of wobbling in improving the spatial resolution of the total-body PET scanner and optimizing acquisition protocols is another path to explore. A major challenge associated with total-body PET is its high cost. This can be addressed by exploring various strategies to reduce the detectors' volume. Reducing the detectors in both the axial and transaxial direction and recovering the missing data through various strategies, including compressed sensing or deep learning approaches will enable building total-body PET scanners with fewer detectors and lower cost, while keeping similar image quality.

5 | CONCLUSION

A total-body PET scanner was modeled using the GATE Monte Carlo toolkit according to the specifications of the uEXPLORER PET scanner. The comparative assessment demonstrated overall good agreement between simulated and experimental performance parameters according to NEMA standards. The impact of the coincidence time window on the NECR was also investigated showing that the use of an optimal coincidence time window along with the maximum ring difference improves the count rate performance. The validated MC model of the uEXPLORER PET scanner enables to investigate different strategies to optimize the performance and potentially reduce the cost.

REFERENCES

1. Zhang X, Zhou J, Cherry SR, Badawi RD, Qi J. Quantitative image reconstruction for total-body PET imaging using the 2-meter long EXPLORER scanner. *Phys Med Biol*. 2017;62(6):2465-2485. doi:10.1088/1361-6560/aa5e46
2. Nadig V, Herrmann K, Mottaghy FM, Schulz V. Hybrid total-body pet scanners-current status and future perspectives. *Eur J Nucl Med Mol Imaging*. 2022;49:445-459. doi:10.1007/s00259-021-05536-4
3. Cherry SR, Jones T, Karp JS, Qi J, Moses WW, Badawi RD. Total-body PET: maximizing sensitivity to create new opportunities for clinical research and patient care. *Journal of Nuclear Medicine*. 2018;59(1):3-12. doi:10.2967/jnumed.116.184028
4. Cherry SR, Badawi RD, Karp JS, Moses WW, Price P, Jones T. Total-body imaging: transforming the role of positron emission tomography. *Sci Trans Med*. 2017;9(381):1-7. doi:10.1126/scitranslmed.aaf6169
5. Rahmim A, Lodge MA, Karakatsanis NA, et al. Dynamic whole-body PET imaging: principles, potentials and applications. *Eur J Nucl Med Mol Imaging*. 2019;46(2):501-518. doi:10.1007/s00259-018-4153-6
6. Zhang X, Xie Z, Berg E, et al. Total-body dynamic reconstruction and parametric imaging on the uEXPLORER. *J Nucl Med*. 2020;61(2):285-291. doi:10.2967/jnumed.119.230565
7. Surti S, Karp J. Impact of detector design on imaging performance of a long axial field-of-view, whole-body PET scanner. *Phys Med Biol*. 2015;60(13):5343-5358. 10.1088/0031-9155/60/13/5343
8. Poon JK, Dahlbom ML, Moses WW, et al. Optimal whole-body PET scanner configurations for different volumes of LSO scintillator: a simulation study. *Phys Med Biol*. 2012;57(13):4077-4094. doi:10.1088/0031-9155/57/13/407
9. Tomasi G, Veronese M, Bertoldo A, Smith CB, Schmidt KC. Substitution of venous for arterial blood sampling in the determination of regional rates of cerebral protein synthesis with L-[1-11C]leucine PET: a validation study. *J Cereb Blood Flow Metab*. 2019;39(9):1849-1863. 10.1177/0271678x18771242
10. Tiwari A, Merrick M, Graves SA, Sunderland J. Monte Carlo evaluation of hypothetical long axial field-of-view PET scanner using GE Discovery MI PET front-end architecture. *Med Phys*. 2022;49(2):1139-1152. doi:10.1002/mp.15422
11. Poon JK. *The performance limits of long axial field of view PET scanners*. PhD Thesis. University of California; 2013.
12. Sheikhzadeh P, Sabet H, Ghadiri H, et al. Development and validation of an accurate GATE model for NeuroPET scanner. *Phys Med*. 2017;40:59-65. doi:10.1016/j.ejmp.2017.07.008
13. Emami A, Ghadiri H, Ghafarian P, Geramifar P, Ay MR. Performance evaluation of developed dedicated breast PET scanner and improvement of the spatial resolution by wobbling: a Monte Carlo study. *Jpn J of Radiol*. 2020;38(8):790-799. doi:10.1007/s11604-020-00966-w
14. Sheikhzadeh P, Sabet H, Ghadiri H, Geramifar P, Ghafarian P, Ay MR. Design, optimization and performance evaluation of BM-PET: a simulation study. *Nucl Instrum*. 2019;940:274-282. doi:10.1016/j.nima.2019.05.083
15. Sanaat A, Arabi H, Ay MR, Zaidi H. Novel preclinical PET geometrical concept using a monolithic scintillator crystal offering concurrent enhancement in spatial resolution and detection sensitivity: a simulation study. *Phys Med Biol*. 2020;65(4):045013. doi:10.1088/1361-6560/ab63ef
16. Ghabrial A, Franklin D, Zaidi H. A Monte Carlo simulation study of the impact of novel scintillation crystals on performance characteristics of PET scanners. *Phys Med*. 2018;50:37-45. doi:10.1016/j.ejmp.2018.05.010
17. Sanaat A, Jamalizadeh M, Khanmohammadi H, Arabi H, Zaidi H. Active-PET: a multifunctional PET scanner with dynamic gantry size featuring high-resolution and high-sensitivity imaging: a Monte Carlo simulation study. *Phys Med Biol*. 2022;67(15):155021. doi:10.1088/1361-6560/ac7fd8
18. Poon JK, MacDonald LR, Cherry SR, Badawi RD. *A simulation study of a long axial field of view whole-body PET scanner using cylindrical and anthropomorphic phantoms*. IEEE; 2008:4999-5006. doi:10.1109/NSSMIC.2008.4774363
19. Crespo P, Reis J, Couceiro M, et al. Whole-body single-bed time-of-flight RPC-PET: simulation of axial and planar sensitivities with NEMA and anthropomorphic phantoms. *IEEE Trans Nucl Sci*. 2012;59(3):520-529. doi:10.1109/TNS.2012.2182677
20. Isnaini I, Obi T, Yoshida E, Yamaya T. Monte Carlo simulation of sensitivity and NECR of an entire-body PET scanner. *Radiol Phys Technol*. 2014;7(2):203-210. doi:10.1007/s12194-013-0253-y
21. Badawi RD, Kohlmyer S, Harrison R, Vannoy S, Lewellen T. The effect of camera geometry on singles flux, scatter fraction and trues and randoms sensitivity for cylindrical 3D PET-a simulation study. *IEEE Trans Nucl Sci*. 2000;47(3):1228-1232. doi:10.1109/23.856575
22. MacDonald L, Harrison R, Alessio A, Hunter W, Lewellen T, Kinahan P. Effective count rates for PET scanners with reduced and extended axial field of view. *Phys Med Biol*. 2011;56(12):3629-3643. doi:10.1088/0031-9155/56/12/011
23. Couceiro M, Ferreira N, Fonte P. Sensitivity assessment of wide axial field of view PET systems via Monte Carlo simulations of NEMA-like measurements. *Nucl Instrum Meth A*. 2007;580(1):485-488.
24. Borasi G, Fioroni F, Del Guerra A, Lucignani G. PET systems: the value of added length. *Eur J Nucl Med Mol Imaging;*. 2010;37:1629-1632. doi:10.1016/j.nima.2007.05.145
25. Eriksson L, Townsend D, Conti M, et al. An investigation of sensitivity limits in PET scanners. *Nucl Instrum Meth A*. 2007;580(2):836-842. doi:10.1016/j.nima.2007.06.112
26. Surti S, Werner M, Karp J. Study of PET scanner designs using clinical metrics to optimize the scanner axial FOV and crystal thickness. *Phys Med Biol*. 2013;58(12):3995-4012. doi:10.1088/0031-9155/58/12/3995
27. Schmall JP, Karp JS, Werner M, Surti S. Parallax error in long-axial field-of-view PET scanners—a simulation study. *Phys Med Biol*. 2016;61(14):5443-5455. doi:10.1088/0031-9155/61/14/5443
28. Ghabrial A, Franklin DR, Zaidi H. A Monte Carlo simulation study of scatter fraction and the impact of patient BMI on scatter in long axial field-of-view PET scanners. *Z Med Phys*. 2021;31(3):305-315. doi:10.1016/j.zemedi.2021.01.006
29. Badawi RD, Shi H, Hu P, et al. First human imaging studies with the EXPLORER total-body PET scanner. *J Nucl Med*. 2019;60(3):299-303. doi:10.2967/jnumed.119.226498
30. Karp JS, Viswanath V, Geagan MJ, et al. PennPET explorer: design and preliminary performance of a whole-body imager. *J Nucl Med*. 2020;61(1):136-143. doi:10.2967/jnumed.119.229997
31. Prenosil G, Sari H, Fürstner M, et al. Performance Characteristics of the Biograph Vision Quadra PET/CT system with long axial field of view using the NEMA NU 2–2018 Standard. *J Nucl Med*. 2022;63(3):476-484. doi:10.2967/jnumed.121.261972
32. Leung EK, Judenhofer MS, Cherry SR, Badawi RD. Performance assessment of a software-based coincidence processor

for the EXPLORER total-body PET scanner. *Phys Med Biol*. 2018;63(18):18NT01. doi:10.1088/1361-6560/aadd3c

33. Lv Y, Lv X, Liu W, et al. Mini EXPLORER II: a prototype high-sensitivity PET/CT scanner for companion animal whole body and human brain scanning. *Phys Med Biol*. 2019;64(7):075004. doi:10.1088/1361-6560/aafc6c

34. Sarrut D, Bała M, Bardiès M, et al. Advanced Monte Carlo simulations of emission tomography imaging systems with GATE. *Phys in Med Biol*. 2021;66(10):10TR03. doi:10.1088/1361-6560/abf276

35. Segars WP, Sturgeon G, Mendonca S, Grimes J, Tsui BM. 4D XCAT phantom for multimodality imaging research. *Med Phys*. 2010;37(9):4902-4915. doi:10.1118/1.3480985

36. OpenGATE Collaboration Users Guide V8. 0 From Wiki Open-GATE.

37. Spencer BA, Berg E, Schmall JP, et al. Performance evaluation of the uEXPLORER total-body PET/CT scanner based on NEMA NU 2–2018 with additional tests to characterize PET scanners with a long axial field of view. *J Nucl Med*. 2021;62(6):861-870. doi:10.2967/jnumed.120.250597

38. Aklan B, Jakoby B, Watson C, Braun H, Ritt P, Quick HH. GATE Monte Carlo simulations for variations of an integrated PET/MR hybrid imaging system based on the Biograph mMR model. *Phys Med Biol*. 2015;60(12):4731-4752. doi:10.1088/0031-9155/60/12/4731

39. Markovsky I, Van Huffel S, Overview of total least-squares methods. *Signal processing*. 2007;87(10):2283-2302. doi:10.1016/j.sigpro.2007.04.004

40. Guez D, Bataille F, Comtat C, Honoré P-F, Jan S, Kerhoas S. Counting rates modeling for PET scanners with GATE. *IEEE Trans Nucl Sci*. 2008;55(1):516-523. doi:10.1109/TNS.2007.910880

41. NEMA Standards Publication NU 2–2018: Performance Measurements of Positron Emission Tomographs. Rosslyn, Virginia, USA. 2018.

42. Stearns CW, McDaniel DL, Kohlmyer SG, Arul PR, Geiser BP, Shanmugam V. Random coincidence estimation from single event rates on the Discovery ST PET/CT scanner. *IEEE Nucl Sci Sym Med Imaging Conf*. 2003:3067-3069. doi:10.1109/NSSMIC.2003.1352545

43. Zein SA, Karakatsanis NA, Issa M, Haj-Ali AA, Nehmeh SA. Physical performance of a long axial field-of-view PET scanner prototype with sparse rings configuration: a Monte Carlo simulation study. *Med Phys*. 2020;47(4):1949-1957. doi:10.1002/mp.14046

44. Salvadori J, Odille F, Verger A, et al. Head-to-head comparison between digital and analog PET of human and phantom images when optimized for maximizing the signal-to-noise ratio from small lesions. *EJNMMI Phys*. 2020;7(1):1-14. doi:10.1186/s40658-020-0281-8

45. Merlin T, Stute S, Benoit D, et al. CASToR: a generic data organization and processing code framework for multi-modal and multi-dimensional tomographic reconstruction. *Phys Med Biol*. 2018;63(18):185005. doi:10.1088/1361-6560/aadac1

46. Thielemans K, Tsoumpas C, Mustafovic S, et al. STIR: software for tomographic image reconstruction release 2. *Phys Med Biol*. 2012;57(4):867-883. doi:10.1088/0031-9155/57/4/867

47. Leung E, Zhang X, Berg E, et al. Relationships between noise-equivalent count rates for extended NEMA NU 2-like scatter phantoms and a human subject scanned using the EXPLORER total-body PET scanner. *J Nucl Med*. 2019;60(1):1385. supplement.